OPEN ACCESS
Journal of Innovative Optical Health Sciences
Vol. 14, No. 3 (2021) 2140012 (9 pages)

DOI: 10.1142/S1793545821400125

World Scientific
www.worldscientific.com

In vivo evaluation of laser-induced choroidal neovascularization in rats simultaneously using optical coherence tomography and photoacoustic microscopy

Fengxian Du*, Lei Gao*, Lin Li†, Qian Li†, Fenghua Wang†,
Chuanqing Zhou†,‡,¶ and Cuixia Dai*,§,¶
*Shanghai Institute of Technology
Shanghai, P. R. China
†Shanghai Jiaotong University
Shanghai, P. R. China
‡zhoucq@sjtu.edu.cn
§sdadai7412@163.com

Received 30 September 2020
Accepted 26 January 2021
Published 6 May 2021

Determination of the precise location and the degree of the Choroidal neovascularization (CNV) lesion is essential for diagnosation Neovascular age-related macular degeneration (AMD) and evaluation the efficacy of treatment. Noninvasive imaging techniques with specific contrast for CNV evaluation are demanded. In this paper, two noninvasive imaging techniques, namely Optical coherence tomography (OCT) and Photoacoustic microscopy (PAM), are combined to provide specific detection of CNV for their complimentary contrast mechanisms. *In vivo* time-serial evaluation of Laser-induced CNV in rats is present at days 1, 3, 5, 7, 14, 21 after laser photocoagulation is applied to the rat fundus. Both OCT and PAM show that the CNV increases to its maximum at day 7 and decreases at day 14. Quantification of CNV area and CNV thickness is given. The dual-modal information of CNV is consistent with the histologic evaluation by hematoxylin and eosin (H&E) staining.

Keywords: Optical coherence tomography; photoacoustic microscopy; medical and biological imaging.

1. Introduction

Neovascular age-related macular degeneration (AMD) is a major cause of vision loss. The hallmark of AMD is Choroidal neovascularization (CNV)[1–3] which is characterized by the abnormal growth of new vessels originating from the choroidal vasculature.[4,5] Through some therapeutic approaches, such as anti-VEGF agents, prevent vision loss in AMD patients, a large proportion of patients with AMD still suffer significant vision impairment.

¶Corresponding authors.

An improved understanding of CNV pathogenesis is still crucial for the prevention and treatment of AMD.

For CNV studies, a laser-induced CNV model in rat or mouse is widely used.[6] Despite its differences from human neovascular AMD, this model has helped to better understand the pathogenesis of CNV and it has been validated in AMD studies and the preclinical testing of most therapeutic approaches.[7] Routinely, the laser-induced CNV in rat or mouse has been evaluated by fluoresceinangiography (FA), which requires the invasive injection of fluorescein. Alternatively, histology and confocal microscopy of immuno-staining in sacrificed animals has been used, which does not allow monitoring the same animal at different times.[8] Currently, Optical coherence tomography (OCT) provides noninvasive, cross-sectional anatomic[9] and functional information of the CNV for clinical and animal studies. In recent years, OCT and its extension technique optical coherence tomography angiography (OCTA) have been widely used in CNV diagnosis.[10–12]

In order to get comprehensive anatomic and functional information of the CNV, several imaging technologies have been combined for multi-modal imaging.[13] Among them, OCT has been integrated with fundus fluorescein angiography (FFA) showing both retinal cross-section and fluorescein imaging.[14,15] Histopathological sections and OCT imaging can clearly demonstrate the positional relationship between the CNV and the retinal pigment epithelium (RPE), and enable quantitative measurement of the CNV.[16] In recent years, OCTA and FA are combined to conduct simultaneous dual-modality retinal vascular imaging.[17] However, these dual-modality techniques suffer from the invasive injection of fluorescein or sacrificing animals. Noninvasive imaging techniques with different specific high contrast for CNV evaluation are preferred. In our previous study, we investigated OCT and photoacoustic microscopy (PAM) for noninvasive, cross-sectional imaging techniques for retinal imaging, demonstrating the integration of PAM with OCT for dual-modality imaging of both optical absorption and scattering contrasts of the retina.[18] Zhangproved PAM be to a noninvasive technique for chorioretinal vasculature imaging[19] and Shuliang Jiao studied ophthalmological imaging simultaneously by using OCT and PAM with a single pulsed broadband light source.[20] Recently, Yannis M. Paulus presented their work on rabbit using OCT and PAM techniques for Retinal Neovascularization imaging.[21] As the performance of this dual-modality system was validated by comparison with conventional multimodal imaging techniques in the evaluation of laser-induced retinal injury and CNV,[22] in this paper, we will present the study of evolution of CNV in rats simultaneously using OCT and PAM techniques.

2. Methods and Materials

2.1. *Experimental system*

A schematic diagram of the experimental system is shown in Fig. 1. A Nd: YAG laser (SPIT-10-100-532,

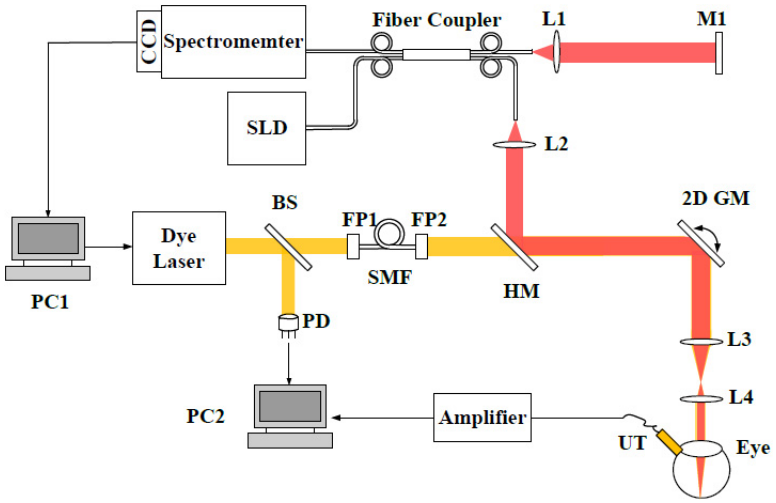

Fig. 1. Schematic of the dual-modal system. PC1, PC2, personal computer. SLD, superluminescent diode. BS, beam splitter. PD, photodiode. FP1, FP2, FiberPort. SMF, singlemode fiber. HM, Hotmirror. 2D GM, two-dimensional galvanometer. UT, ultrasonic transducer. M1, mirror. L1–L4, lens.

El for light Ltd., Daventry, U.K.; pulse duration < 2 ns; pulse repetition rate > 10 kHz) was used as the illumination source for PAM. The laser output was delivered by a single-mode optical fiber and was further collimated. A galvanometer (TSH8203M, Century Sunny Technology CO., LTD, China) scanned the laser beam and delivered the light onto the retina using a telescope configuration. The induced PA signals from the retina were detected by a customized ultrasonic transducer (30 MHz central frequency, 15 MHz bandwidth, $0.5 \times 0.5\,\text{mm}^2$ active element size), which was placed in contact with the eyelid coupled by ultrasound gel. The detected PA signals were amplified by 56 dB and were digitized by a data acquisition board (Compuscope14200, Gage) at a sampling rate of 200 MS/s. The laser pulse energy was 60 nJ, which was safe for rat eyes.[18–20]

A fiber-based SD-OCT was integrated with PAM. It consisted of a broadband light source (IPSDD0804, In Phenix, CA; center wavelength: 840 nm; 6-dB bandwidth: 50 nm), a 50×50 single-mode fiber coupler, a reference arm, a sample arm coupled with the PAM by a dichroic mirror (Edmund Optics, 45 DEG 50 MM SQ)with the illumination powers 0.8 mW, and a homebuilt spectrometer which consisted of a grating (Wasatch, 1800 lines/mm), a focusing lens (Thorlabs, focal length:100 mm), and a line camera (Aviiva SM2, e2v). The axial resolution of PAM and SD-OCT was quantified to be 35 μm and 6.4 μm, respectively. Both SD-OCT and PAM were shown to have comparable lateral resolution (20 μm) when imaging the rat retina *in vivo*.

In simultaneous OCT and PAM imaging, we performed 256 A-lines in each B-scan and scanned 256 discrete B-scan positions to produce a volumetric map of the retinal and choroidal imaging. The final image volume of data is $256 \times 256 \times 2048$ pixels (x-256, y-256, z-2048). Both OCT and PAM had the same B-scan frame rate which was 19.5 frame/s, and it took 13 s to acquire the entire image volume. In data processing, OCT *en face* images generated from the acquired 3D OCT dataset, and PAM *en face* images was produced from the maximum-amplitude projection (MAP) of the dataset.

2.2. *Animals*

In our study, Laser-induced rupture of Bruch's membrane in Brown Norway rat was used as the CNV animal model. We performed laser photocoagulation to rupture Bruch's membrane in the eye of Brown Norway rat (20 male rats and 10 female rats, 8–10 weeks) with an Argon 532 nm laser (IRIDEX OculightGLx, spot size: 50 μm, output duration:100ms, output power: 200 mw in our treatment) which was attached to a slit lamp delivery system (30SL-M, Carl Zeiss). During laser treatment, a glass cover slip was used to flatten the cornea and the laser beam was focused onto the retina. Successful laser applications resulted in "bubble" formation during photocoagulation.

During experiments, we used a mixture of isoflurane with compressed normal air to anesthetize rats. Before imaging, we dilated the rodents' pupils with a 1% tropicamide ophthalmic solution and paralyzed the iris sphincter muscle with a 0.5% tetracaine hydrochloride ophthalmic solution. Artificial teardrops (Systane, Alcon Laboratories, Inc.) were applied every other minute to prevent corneal dehydration. Anesthetized animals were restrained in a home-built holder, which was placed on an adjustable platform with five degree of freedom.

2.3. *Histology*

For histological analysis, rats were sacrificed and eyes were dissected and fixed in 4% paraformaldehyde (PFA) in phosphate buffer saline (PBS) at 4°C for 24 h, dehydrated in a dehydrator JJ-12J (Junjie, Wuhan, China), and embedded in paraffin using JB-P5 (Junjie, Wuhan, China). Retinal sections were cut at a thickness of 4 μmon a microtome (RM2016; Leica Biosystems, St. Louis, MO, USA), and then stained with haematoxylin and eosin (H&E). Images were obtained using a light microscope (BX51, Olympus, Tokyo, Japan).

3. Results

3.1. *Simultaneous OCT and PAM findings in normal retina and laser-induced CNV in rats*

As shown in Fig. 2 in which the OCT and PAM images were simultaneously obtained, discrepancies between the normal retina and the laser-induced CNV retina (7 days after laser photocoagulation) can be obviously differentiated.

OCT *en face* image from the normal retina presented a photograph of health fundus. For a laser-induced CNV eye, the lesion area in the OCT image

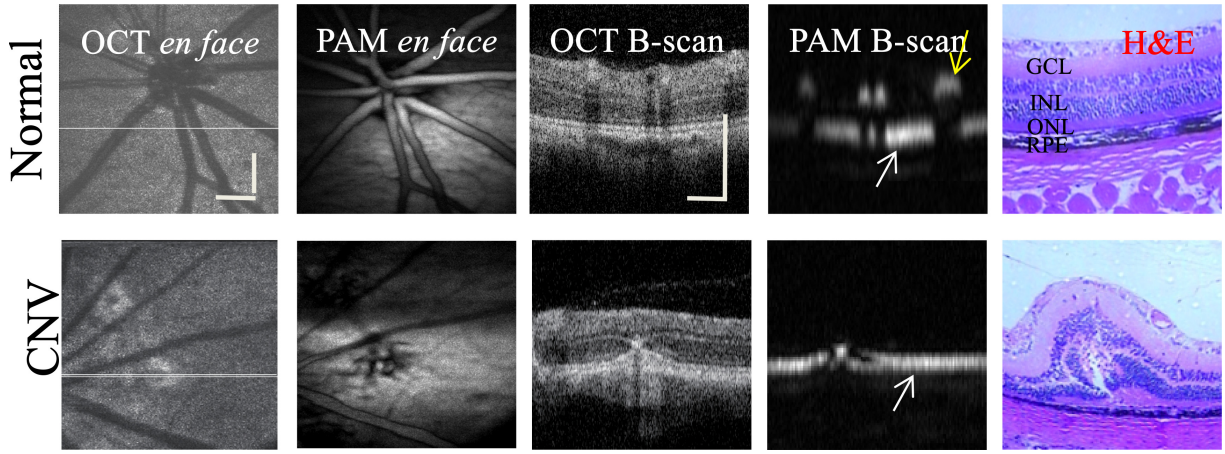

Fig. 2. Dual-modal imaging of normal retina and laser-induced CNV and comparison with histopathological images. GCL, ganglion cell layer. INL, inner nuclear layer. ONL, outernuclear layer. RPE, retinal pigment epithelium. White arrows point to the RPE layer and the yellow arrow points to the vessel above the RPE layer. Bar: 120 μm.

appeared grayish white. OCT B-scan image from the normal retina showed high reflection from the inner layers and a weak reflection from the outer layers. The retinal pigment epithelium (RPE) and choriocapillaris were observed as triple bands of high reflection. In the laser-induced CNV image, the choriocapillaris hyperreflective subretinal lesion was easily differentiated from the surrounding retina and subretinal hyporeflective areas. An irregular, multi-layered, highly reflective area thatprotruded into the subretinal space above the disruption of the highly reflective RPE layer appeared in the OCT image.

In the PAM *en face* and cross-sectional images, in which high absorption contrast of vessels and RPE layer was provided, the normal retina showed regular image of vessels and RPE layer, and the laser-induced CNV fundus showed obvious information of neovascularization. Detail distribution of new vessels over the laser photocoagulation region was clearly shownin the *en face* PAM image, and the B-scan image showed the neovacular protruded into subretinal space and high above the RPE layer.

Compared with the paraffin sections, in which choroid and intraretinal layers were recognized, intraretinallayers recognized in OCT B-scan images with high resolution matched with the histologic evaluation and information of vessels and RPE layer were proved by the PAM cross-sectional images. Normal retina OCT image provided the inner highly reflective layer corresponding with the inner retinallayers including the nerve fiber layer (NFL), ganglion cell layer (GCL), inner plexiform layer (IPL), inner nuclear layer (INL), outer plexiformlayer (OPL) and the outer low-reflective layer corresponds with the outernuclear layer (ONL) and the photoreceptor layer. PAM cross-sectional image showed the regular vessels and holonomic RPE layer except position where light was blocked by the vessels. Paraffin sections image of the laser-induced CNV retina showed the elevated sensory retina and a large number of hemosiderin-laden macrophages and thick fibrovascular membranes with many fibroblasts and new vessels could be observed. In the dual-modal performance, OCT B-scan image obviously showed subretina neovascularization and PAM B-scan image showed the neovascularizationdegree up above the RPE layer.

3.2. *Dual-modal images of laser-induced CNVand correlation with histology over time*

Simultaneous OCT and PAM of time-serial imaging of CNV are shown in Fig. 3.

On day 1, as shown in the OCT image, there was a disruption of the highly reflective RPElayer in the center of the lesion, and the extension of the reflective area of sensory retinainto the choroid through the disrupted site of the RPE. The reflection corresponding to the choroid was enhanced and thickened at the outer site of this disruption. As shown in the light absorption in the PAM image, there was a hole on the PAM image as a result of Bruch's membrane being ruptured by laser photocoagulation. The dual-modal images could be

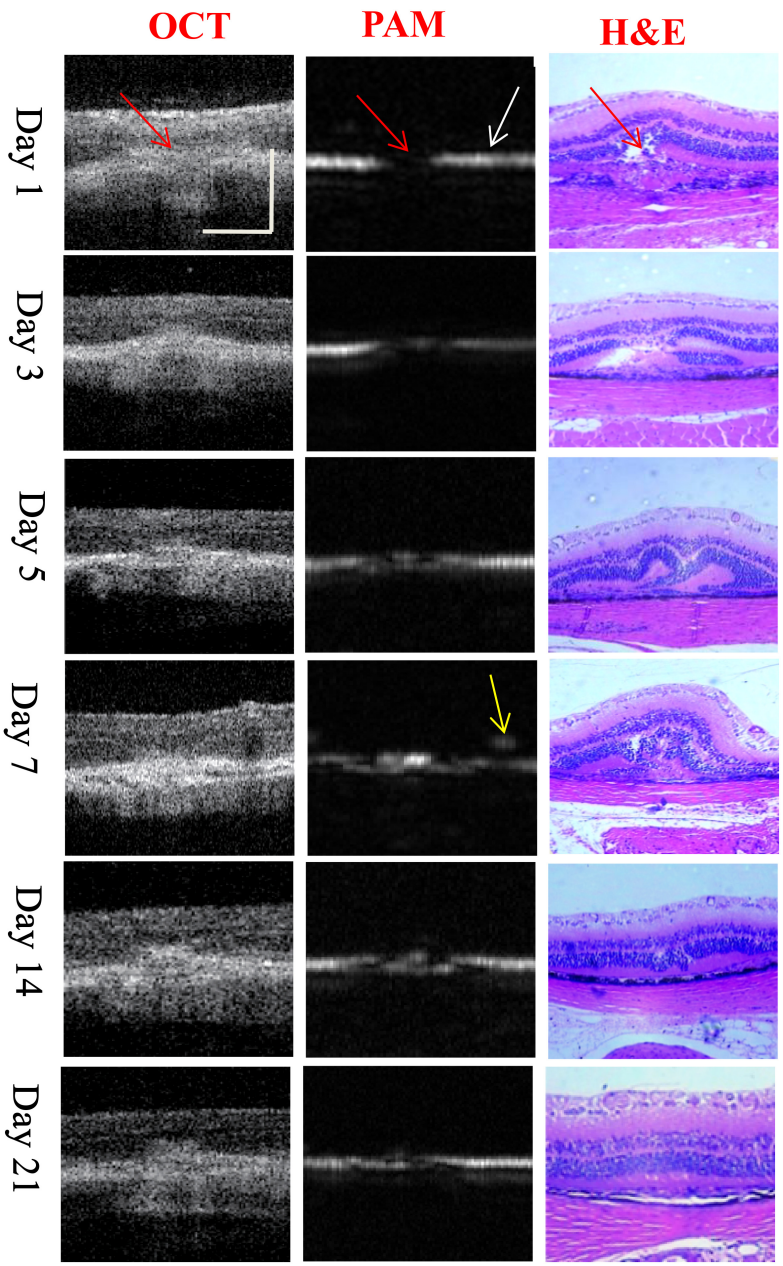

Fig. 3. Evaluation of laser-induced CNV evolutionusing OCT and PAM and comparison with histopathological images. Red arrows point to the CNV Region, white arrow points to the RPE layer and the yellow arrow points to the vessel above the RPE layer. Bar: 50 μm

validated by the histopathology. In the histologic evaluation of H&E staining, a disruption of both RPE and Bruch's membrane in the center of the lesion-could be seen. The inner and outer segments of the photoreceptor cells appeared as a coagulative necrosis. The outer nuclear layer extended into the choroid through the disrupted site of Bruch's membrane.

On day 3, the OCT image showed that the swelling decreased and became less reflective in its inner part. The OPL folded toward the ONL and increased reflectivity in the RPE and the outer photoreceptor region was observed. In the PAM image, weak absorption was observed at the disruption position of the RPE layer which represented that new capillaries came into being. This corresponded to the progression of the injury and the wound-healing response seen in H&E stained image, and the CNV membrane was seen as a protrusion growing into the under-retinal area.

On day 5, thick, higher reflectivity appeared near the RPE layer region indicating more vessels grew in the under-retinal region in the OCT image. More

absorption shown in the PAM image indicated the CNV became much serious. Stronger absorption nearly covered the whole disruption position. H&E stained image indicated CNV extended from the choroid into the subretinal space. Then arrow CNV tissue consisted mainly of immature vascular-endothelial cells and spindle-shaped RPE cells.

On day 7, anelevation of the sensory retina and highly reflective area in the subretinal space could be seen in the OCT image. Highly reflective area was also seen under the sensory retina. The CNV increased to its maximum size. As seen from the PAM image, the CNV grew above the RPE layer and new vessels protrusion into sub retinal region were obviously detected. The CNV increased to its maximum size also showed in PAM image. In the H&E staining image, the sensory retina was elevated to be a dome shape. A large number of hemosiderin-laden macrophages and thick fibrovascular membranes with many fibroblasts and new vessels could be observed. The maximum CNV size on day 7 was proved in H&E stained sections.

SD-OCT revealed that the size of the sub retinal lesion decreased on day 14 and a continuing decreased in CNV size on day 21. Therefore, the hyper-reflective site was blurred with less reflectivity in SD-OCT images. The folded OPL returned to be normal in SD-OCT and H&E stained images, but the photoreceptor layer remained to be adis continuous hyper-reflective line. The PAM images showed the decreased absorption which was consistent with the OCT information and the H&E staining (Fig. 3, days 14 and 21).

Comparing with the OCT, PAM and H&E stained sections, in which the scattering information was given from the OCT images and the absorption contrast was given in PAM image, it could be seen that information of OCT and PAM was verified by Histology images.

3.3. *Time-serial dual-modal imaging of the same laser-induced CNV lesion*

Figure 4 shows the time-serial imaging of the same CNV lesion. OCT *en face* images showed a gray spot in the area corresponding to the laser photocoagulation, no obvious change could be found during the CNV evolution. Details of CNV evolution were given in the OCT B-scan images: the retina showed a variable amount of swelling and an increase in reflectivity within the first three days. Hyperreflective reaction was observed originating from the RPE and the outer photoreceptor layer and from the inner part of the photoreceptors and the outer plexi form layer. Higher reflection was observed on day 5 and day 7. The CNV increased to its maximum size on day 7 and the lesion exhibited a crater-like configuration with development of neovascularization growing into the sub retinal layer. OCT B-scan image revealed that the size of the sub retinal lesion decreased on day 14 and the hyper-reflective site was blurred with less reflectivity.

PAM *en face* image provided complementary details of the CNV evolution. Absorption contrast at the lesion area shown in the *en face* images showed disruption of laser photocoagulation on day 1 and the new capillaries growing fast inside the lesion area and increasing to its maximum on day 7 and decreasing on day 14. Details of CNV at the center and the border of the lesion could be clearly differentiated. Neovascularization degree growing from the lesion, at the RPE layer and into the sub retinal area could be detected in the B-scan images.

3.4. *In vivo quantification of size in laser-induced CNV*

As shown in the above OCT and PAM images, OCT *en face* images showed no obvious change during the CNV evolution but the PAM *en face* images showed details of CNV spreading over the lesion area. New capillaries growing from the choroid up to sub retina could be differentiated in the PAM B-scan images at 35μm axial resolution but highreflectivityin the OCT B-scan images clearly showed CNV tissue with high resolution. We can calculate the size of CNV from PAM *en face* images and the OCT B-scan images. In this study, Image analysis software ImageJ was used to calculate the thickness size and the area of each CNV.

In OCT B-scan images, the CNV was evaluated by the thickness of CNV which was defined as the maximum thickness of highly reflective layer above the RPE in the section passing through the center of the CNV (the center of the lesion was defined as the midline passing through the area of RPE-Bruch's-membrane rupture). Lesion area in PAM *en face* images was also calculated to evaluate the CNV process.

Thickness and area of CNV were calculated on days 3, 5, 7, 14, and 21. As shown in Fig. 5,

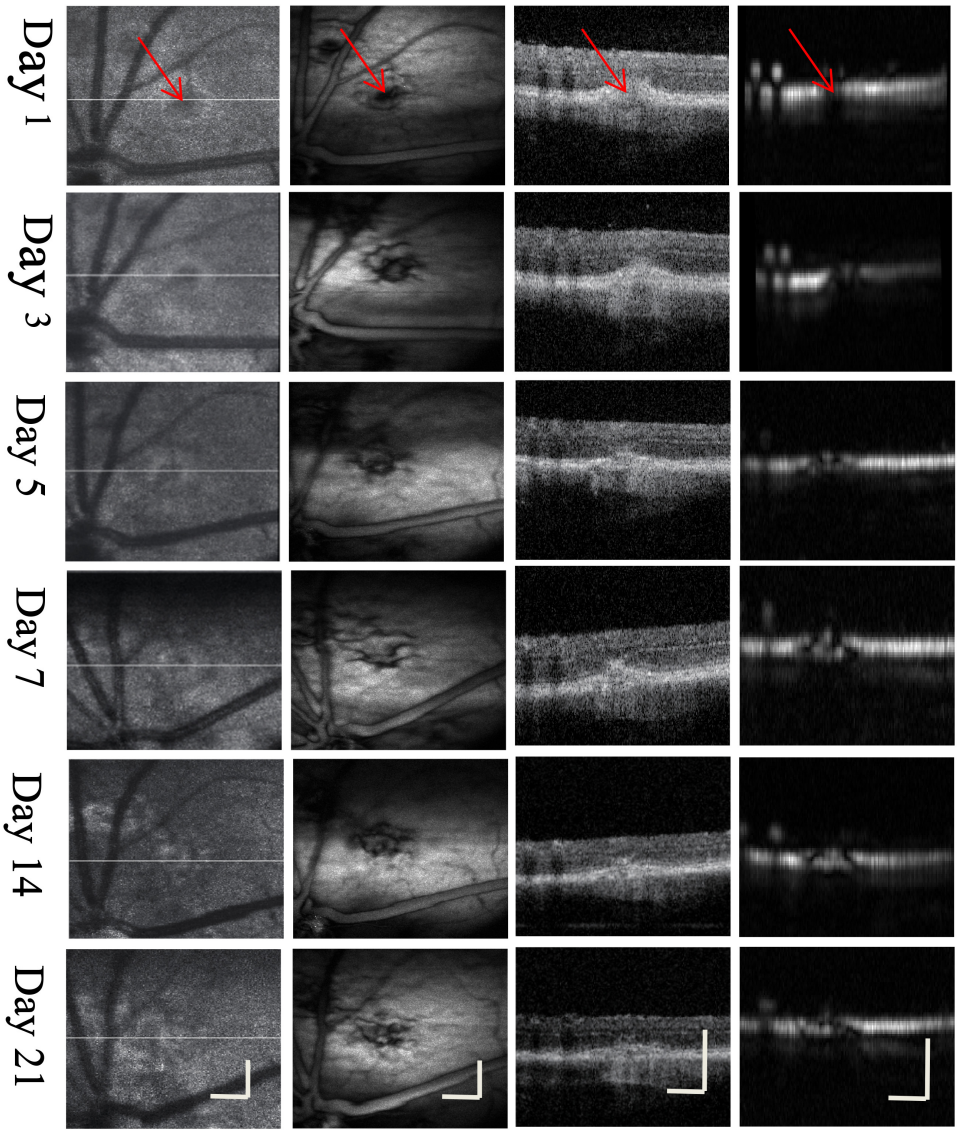

Fig. 4. CNV evolution of the same lesion imaged withdual-modal OCT and PAM system. From left to right: OCT*en face*, PAM *en face*, OCT B-scan, PAM B-scan. Red arrows point to the CNV region. Bar: 120μm

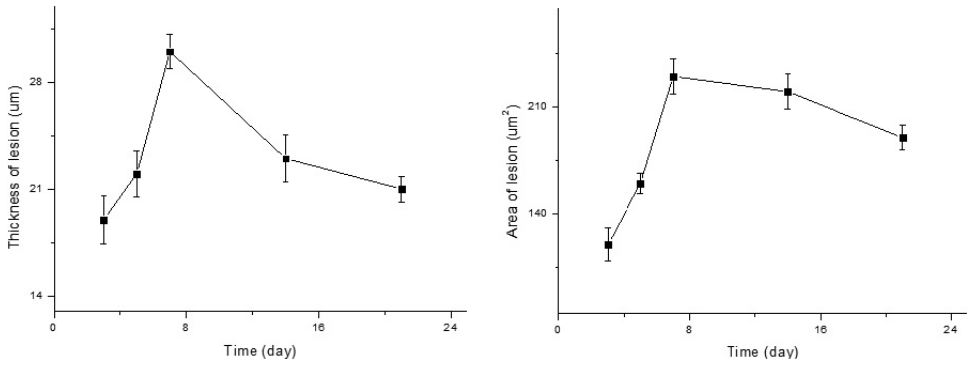

(a) (b)

Fig. 5. *In vivo* evaluation of CNV size (a) Thickness of lesion calculated from the OCT B-scan images (b) Area of lesion calculated from PAM *en face* images. Data expressed as mean $\pm$ SD ($N = 6$, $p < 0.01$).

measurement of the thickness and area of lesion revealed that CNV reached a peak on day 7 and rapidly decrease afterward, reaching a minimum on day 21. CNV increased significantly from day 5 to day 7 and decreased from day 7 to day 21. The biggest decline in size was observed between day 7 and day 14.

4. Discussion and Conclusion

SD-OCT provides *invivo* anatomical details of choroidal/retinal lesions and PAM images give the complementary information of light absorption. In this paper, we demonstrated the entire development process of laser-induced CNV in rat simultaneously using these two noninvasive techniques. We also monitored the pathological features of CNV development using histology. The dual-modal images correlated with the histologic evaluation. We were able to identify three stages in this process that included an initial early reaction phase, a phase of neovascular proliferation, and a stage that involved the regression of the neovascular complex.

OCT *en face* images can be used to detect the location of lesion but cannot provide the degree of CNV. However, PAM *en face* images can give details of CNV spreading over the lesion area. Combination with complementary information provided by OCT B-scan and PAM B-scan, the CNV thickness and new capillaries growing from the choroid up to sub retina can be obviously differentiated. Another important application of this study is that OCT and PAM allowed the assessment of the CNV size. This methodology is fast and reliable.

Recently, OCTA grows fast and is applied in CNV detection. OCT combining OCTA can give detail information of CNV. However, no time-serial evaluation of CNV has been reported. It will be valuable and promising to study the CNV by simultaneously using OCT, OCTA, and PAM techniques.

In conclusion, our study provides evidence that dual-modal OCT and PAM is a valuable tool for the *in vivo* evaluation of the laser-induced CNV model in rat. Information of OCT and PAM of CNV lesion reveals morphologic features that are common to human pathology. This study will laid in better understanding of CNV pathogenesis.

Conflict of Interest

The authors declare to have no conflict of interest.

Acknowledgments

This work was supported by the Natural National Science Foundation of China (Grant Nos. 61675134, 61307015, 81827807 and 68175123), Science and Technology innovation project of Shanghai Science and Technology Commission (19441905800), Project of State Key Laboratory of Ophthalmology, Optometry and Visual Science, Wenzhou Medical University (K181002). Fengxian Du and Lei Gao are the co first authors for this paper.

References

1. K. Attebo, P. Mitchell, W. Smith, "Visual acuity and the causes of visual loss in Australia: The Bluemountains Eye Study," *Ophthalmology* **103**, 357–364 (1996).
2. D. S. Friedman, B. J. O'Colmain, B. Munoz *et al.*, "Prevalence of agerelated macular degeneration in the United States," *Arch Ophthalmol.* **122**, 564–572 (2004).
3. M. R. VanNewkirk, M. B. Nanjan, J. J. Wang, P. Mitchell, H. R. Taylor, C. A. McCarty, "The prevalence of age-related maculopathy: The Visual Impairment Project," *Ophthalmology* **107**, 1593–1600 (2000).
4. C. Augood, A. Fletcher, G. Bentham, U. Chakravarthy, P. T. de Jong, M. Rahu, J. Seland, G. Soubrane, L. Tomazzoli, F. Topouzis, J. Vioque, I. Young, "Methods for a population-based study of the prevalence of and risk factors for age-related maculopathy and macular degeneration in elderly European populations: The EUREYE study," *Ophthalmic Epidemiol.* **11**, 117–129 (2004).
5. J. Ambati, B. K. Ambati, S. H. Yoo, S. Ianchulev, A. P. Adamis, "Age-related macular degeneration: Etiology, pathogenesis, and therapeutic strategies," *SurvOphthalmol.* **48**, 257–293 (2003).
6. S. H. Zhao, S. Z. He, "Study on the experimental model of krypton laser-induced choroidal neovascularization in rats," *Zhonghua Yan Ke Za Zhi.* **39**, 298–302 (2003).
7. H. Y. Hou, H. L. Liang, Y. S. Wang, "Bone marrow-derived cells in neovascular age-related macular degeneration: Contribution and potential application," *Ophthalmic Res.* **45**, 1–4 (2011).
8. I. Semkova, S. Fauser, A. Lappas, N. Smyth, N. Kociok, B. Kirchhof, M. Paulsson, V. Poulaki, A. M. Joussen, "Overexpression of FasL in retinal pigment epithelial cells reduces choroidal neovascularization," *FASEB J.* **20**, 1689–1691 (2006).

9. Z. H. Yang, J. W. Shang, C. L. Liu, J. Zhang, F. Hou, Y. M. Liang, "Intraoperative imaging of oral-maxillofacial lesions using optical coherence tomography," *J. Innov. Opt. Health Sci.* **13**(2), 2050010 (2020).
10. D. Ferrara, N. K. Waheed, J. S. Duker, "Investigating the choriocapillaris and choroidal vasculature with new optical coherence tomography technologies," *Prog. Retinal Eye Res.* **52**, 130–155 (2016).
11. R. X. Chen, L. Yao, K. Y. Liu, T. T. Cao, H. K. Li and P. Li, "Improvement of decorrelation-based OCT angiography by an adaptive spatial-temporal kernel in monitoring stimulus-evoked hemodynamic responses," *IEEE Trans. Med. Imaging.* **39**, 4286–4296 (2020), doi: 10.1109/TMI.2020.3016334.
12. L. Huang, Y. Fu, R. Chen, S. Yang, H. Qiu, X. Wu, S. Zhao, Y. Gu and P. Li, "SNR-adaptive OCT angiography enabled by statistical characterization of intensity and decorrelation with multi-variate time series model," *IEEE Trans. Med. Imag.* **38**, 2695–2704 (2019).
13. W. Qiao, Z. J. Chen, "All-optically integrated photoacoustic and optical coherence tomography: A review," *J. Innov. Opt. Health Sci.* **10**, 1730006 (2017).
14. J. L. Edelman, M. R. Castro, "Quantitative image analysis of laser-induced choroidal neovascularization in rat," *Exp. Eye Res.* **71**, 523–533 (2000).
15. T. Fukuchi, K. Takahashi, K. Shou, M. Matsumura, "Optical coherence tomography (OCT) findings in normal retina and laser induced choroidal neovascularization in rats," *Graefes Arch. Clin. Exp. Ophthalmol.* **239**, 41–46 (2001).
16. J. Jiao, B. Mo, H. Wei, Y. R. Jiang, "Comparative study of laser-induced choroidal neovascularization in rats by paraffin sections, frozen sections and high-resolution optical coherence tomography," *Graefes Arch. Clin. Exp. Ophthalmol.* **251**, 301–307 (2013).
17. T. Liu, L. Hui, Y. S. Wang, J. Q. Guo, R. Li, J. B. Su, J. K. Chen, X. M. Xin, W. H. Li, "In-vivo investigation of laser-induced choroidal neovascularization in rat using spectral-domain optical coherence tomography (SD-OCT)," *Graefes Arch Clin Exp Ophthalmol.* **251**, 1293–1301 (2013).
18. L. Li, C. X. Dai, C. Q. Zhou, "Fast subcellular optical coherence photoacousticmicroscopy for pigment cell imaging," *Opt. Lett.* **40**, 4448–4451 (2015).
19. Q. Wei, T. Liu, S. L. Jiao, H. F. Zhang, "Image chorioretinal vasculature in albino rats using photoacoustic ophthalmoscopy," *J. Mod. Optic.* **58**, 1997–2001 (2011).
20. X. J. Liu, T. Liu, R. Wen, Y. W. Li, C. A. Puliafito, H. F. Zhang, S. L. Jiao, "Optical coherence photoacoustic microscopy for in vivo multimodal retinal imaging," *Opt. Lett.* **40**, 1370–1373 (2015).
21. V. P. Nguyen, Y. X. Li, M. Aaberg, W. Zhang, X. D. Wang, Y. M. Paulus, "In vivo 3D imaging of retinal neovascularization using multimodal photoacoustic microscopy and optical coherence tomography imaging," *J. Imaging* **4**, 1–18 (2018).
22. M. C. Xiao, C. X. Dai, L. Li, C. Q. Zhou, F. H. Wang, "Evaluation of retinal pigment epithelium and choroidal neovascularization in rats using laser-scanning optical-resolution photoacoustic microscopy," *Ophthalmic Res.* **63**, 271–283 (2020).